



# Adjustable core-sheath architecture of polyaniline-decorated hollow carbon nanofiber nanocomposites with negative permittivity for superb electromagnetic interference shielding

Xiaojiang Xu<sup>1</sup> · Feichong Yao<sup>1</sup> · Ola A. Abu Ali<sup>2</sup> · Wenhao Xie<sup>1</sup> · Samy F. Mahmoud<sup>3</sup> · Peitao Xie<sup>4</sup> · Salah M. El-Bahy<sup>5</sup> · Mina Huang<sup>6</sup> · Chuntai Liu<sup>7</sup> · Runhua Fan<sup>4</sup> · Zhanhu Guo<sup>10</sup> · Ai Du<sup>8</sup> · Diana Estevez<sup>9</sup> · Faxiang Qin<sup>9</sup> · Huaxin Peng<sup>9</sup> · David P. Young<sup>11</sup> · Hongbo Gu<sup>1</sup>

Received: 12 May 2022 / Revised: 23 June 2022 / Accepted: 7 August 2022 / Published online: 18 August 2022  
© The Author(s), under exclusive licence to Springer Nature Switzerland AG 2022

## Abstract

In this work, the adjustable core-sheath architecture in the hollow carbon nanofibers/polyaniline (HCNFs/PANI) nanocomposites with negative permittivity and an outstanding electromagnetic interference (EMI) shielding performance have been developed. The effect of thickness for polyaniline sheath on the electrical property and EMI performance of HCNFs/PANI nanocomposites has been studied in detail. The results demonstrate that the highest electrical conductivity of  $22.71 \pm 0.10$  S cm<sup>-1</sup> and the largest EMI shielding effectiveness (SE) of 60–94 dB within the X-band range (8.0–12.4 GHz) is observed in the HCNFs/PANI nanocomposites with a HCNFs loading of 50 wt%. The excellent electrical conductivity, a changeable dielectric resonance from positive to negative in the X-band range, and the internal multiple scattering at interfaces between HCNFs and PANI are devoted to this unique EMI shielding performance in HCNFs/PANI nanocomposites. This work enables a new approach to create the novel structural polymeric materials with negative permittivity for EMI shielding.

**Keywords** Hollow carbon nanofibers · Polyaniline · Negative permittivity · Electrical conductivity · Internal multiple scattering · EMI shielding

---

Xiaojiang Xu and Feichong Yao contributed equally.

✉ Hongbo Gu  
hongbogu2014@tongji.edu.cn

<sup>1</sup> Shanghai Key Lab of Chemical Assessment and Sustainability, School of Chemical Science and Engineering, Tongji University, Shanghai 200092, China

<sup>2</sup> Department of Chemistry, College of Science, Taif University, P.O. Box 11099, Taif 21944, Saudi Arabia

<sup>3</sup> Department of Biotechnology, College of Science, Taif University, P.O. Box 11099, Taif 21944, Saudi Arabia

<sup>4</sup> College of Ocean Science and Engineering, Shanghai Maritime University, Shanghai 201306, China

<sup>5</sup> Department of Chemistry, Turabah University College, Taif University, P.O. Box 11099, Taif 21944, Saudi Arabia

<sup>6</sup> College of Materials Science and Engineering, Taiyuan University of Science and Technology, Taiyuan 030024, China

<sup>7</sup> Key Laboratory of Materials Processing and Mold (Zhengzhou University), Ministry of Education, National Engineering Research Center for Advanced Polymer Processing Technology, Zhengzhou University, Zhengzhou, People's Republic of China

<sup>8</sup> Shanghai Key Laboratory of Special Artificial Microstructure Materials and Technology, School of Physics Science and Engineering, Tongji University, Shanghai 200092, People's Republic of China

<sup>9</sup> Institute for Composites Science Innovation (InCSI), School of Materials Science and Engineering, Zhejiang University, Hangzhou 310027, People's Republic of China

<sup>10</sup> Department of Physics and Astronomy, Louisiana State University, Baton Rouge, LA 70803, USA

<sup>11</sup> Integrated Composites Lab (ICL), Department of Chemical & Biomolecular Engineering, University of Tennessee, Knoxville, TN 37966, USA

## 1 Introduction

With the development of smart electronics and modern information technology, electromagnetic pollution has become a serious problem faced by humanity. Consequently, more efforts have been dedicated to the design and exploitation of new structural materials with a high efficiency of electromagnetic interference (EMI) shielding [1, 2]. Usually, metals are used for effectively shielding electromagnetic (EM) waves because of their high electrical conductivity (normally  $10^4$ – $10^5$  S  $\text{cm}^{-1}$ ) [3]. However, high density, poor corrosion resistance, and difficulty in processing limit their deployments in the EMI shielding field [4]. Lately, highly electrically conductive polymer-based composites composed of polymer matrix and conductive fillers are becoming the research focus and have been intensively studied for EMI shielding due to their advantages such as lightweight, corrosion resistance, high flexibility, and easy processing [5, 6]. Generally, EMI shielding performance of polymer-based composites depends on the dispersion quality of fillers within the polymer matrix, the interfaces between polymer matrix and fillers, and the microstructures of composites [7].

According to Maxwell's equations, EMI shielding is associated with the material's permittivity and permeability. Hence, due to the unique electromagnetic properties, artificially manufactured metamaterials with a negative refractive index, including negative permittivity (negative  $k$ ) and/or negative permeability (negative  $\mu$ ) at certain frequencies, are recently illustrated as promising candidates for EMI shielding in electronic devices [8, 9]. Since the size of microstructures is smaller than the wavelength of EM waves, the metamaterials are able to interact with EM waves through blocking, absorbing, or bending, further suppressing the waves and probably achieving an effective EMI shielding performance [10].

Different from the traditional metamaterials with artificially designed periodic structures, negative electromagnetic parameters are recently reported in the polymer nanocomposites with random structures, which are called metacomposites, including polypyrrole/tungsten oxides [11], polydimethylsiloxane/multi-walled carbon nanotubes (PDMS/MWCNTs) [12], elastomer/carbon nanofibers [13], epoxy/barium ferrite [14], polyimide/MWCNTs [15], and so on. These negative parameters are capable of being tailored by the filler loadings, morphology, and surface functionality [16]. Most notably, negative permittivity was found in the polyaniline (PANI) and its nanocomposites [17]. Negative permittivity in PANI is ordinarily linked to its intrinsic nature and continuous conductive network in its polymer chain [18]. This special feature might give rise to the possibility of PANI and its nanocomposites in the

EMI shielding field. Additionally, the formation of internal scatterings at multiple interfaces is considered as a way to realize the superior EMI shielding performance for a material since the multiple interface is able to produce the internal scatterings of EM waves in the inner part of a material, which is favorable for further absorption and attenuation of EM waves [19].

Based on these strategies, in this work, the hollow carbon nanofibers (HCNFs) and PANI (doped with *p*-toluene sulfonic acid, PTSA) have been selected to construct a core-sheath structure for building a HCNFs/PANI nanocomposite with the internal multiple interfaces, as depicted in the inset of Fig. 2B. The structures of HCNFs/PANI nanocomposites have been determined by Fourier-transform infrared (FTIR), scanning electron microscope (SEM), transmission electron microscopy (TEM), Raman spectroscopy, and ultraviolet–visible diffuse reflectance spectroscopy (UV–vis DRS). These HCNFs/PANI nanocomposites illustrate an excellent EMI shielding effectiveness (SE) in the X-band range (8.2–12.4 GHz) at a thickness of 2.00 mm measured on a vector network analyzer and a negative permittivity within the same frequency range. This work aims to provide a new method for design and development of polymer nanocomposites for EMI shielding.

## 2 Experimental section

### 2.1 Materials

The hollow carbon nanofibers (HCNFs,  $D \times L$ : 100 nm  $\times$  20–200  $\mu$  m, average pore volume: 0.075  $\text{cm}^3 \text{g}^{-1}$ ) were obtained from Sigma Aldrich. Aniline ( $\text{C}_6\text{H}_7\text{N}$ ,  $\geq 98\%$ ) was obtained from Aladdin Reagent Co., Ltd. Anhydrous ethanol ( $\text{C}_2\text{H}_5\text{OH}$ ,  $\geq 99.7\%$ ), *p*-toluene sulfonic acid (PTSA,  $\text{C}_7\text{H}_8\text{O}_3\text{S}$ , 99%), and ammonium persulfate (APS,  $(\text{NH}_4)_2\text{S}_2\text{O}_8$ ,  $\geq 98.5\%$ ) were purchased from Shanghai Macklin Biochemical Co., Ltd. Dichromate ( $\text{K}_2\text{Cr}_2\text{O}_7$ ,  $\geq 99.8\%$ ) was supplied by Sinopharm Chemical Reagent Co., Ltd. All the chemical reagents were used directly without any further treatment.

### 2.2 Fabrication of HCNFs/PANI metacomposites

HCNFs/PANI nanocomposites were fabricated with a surface-initiated polymerization (SIP) method. First, the HCNFs were dispersed in 100 mL of Cr(VI) solution (50 mg  $\text{L}^{-1}$ ) by 15 min under sonication. Then the treated HCNFs were filtered and washed by deionized water for 3 to 5 times to remove the residual Cr(VI). Then, the treated HCNFs were dispersed in 80 mL of deionized water, and the aniline (18 mmol) was added into this suspension slowly under

sonication with mechanical stirring in an ice-water bath for 1 h. The PTSA (15 mmol) and the APS (9 mmol) were dissolved in 20 mL of deionized water and then mixed with the above mixture. The mixture was maintained for additional 2 h under sonication with mechanical stirring in an ice-water bath for further polymerization. Afterward, the product was vacuum filtered and rinsed with deionized water and ethanol for 5 times, respectively, to remove any possible impurity or oligomers. The final HCNFs/PANI nanocomposites were dried in a freeze-dryer for 24 h. The preparation diagram is shown in Scheme S1. The HCNFs/PANI nanocomposites with a HCNF loading of 10, 20, 40, and 50 wt% were fabricated. In comparison, the pure PANI was also fabricated following the above procedures without adding HCNFs.

### 2.3 Characterizations

A field emission SEM (S-4800) and a TEM (Tecnai G20) were used to observe the microstructures of samples. XRD was conducted on a D8 Advance X-ray powder diffractometer within the diffraction angle ranges from 10 to 70° at a scanning speed of 10° min<sup>-1</sup>. The FTIR spectra of samples were recorded on a Thermo Nicolet NEXUS with an attenuated total reflection (ATR) accessory (Thermo Scientific) in the range of 400–4000 cm<sup>-1</sup>. Raman spectra were motivated in the visible range with a He–Ne for the 633-nm laser and collected on a Renishaw inVia Reflex Raman spectrometer. The thermogravimetric analysis (TGA) was recorded by a SDT thermal-microbalance apparatus at a heating rate of 20 °C min<sup>-1</sup> within a temperature range from 25 to 1000 °C with an air flow rate of 20 mL min<sup>-1</sup>. The UV–vis DRS was performed on a Cary 5000 instrument.

The EMI shielding characteristics were determined by measuring the values of complex scattering parameters (*S* parameters) of the reflection (*S*<sub>11</sub> or *S*<sub>22</sub>) and the transmission (*S*<sub>12</sub> or *S*<sub>21</sub>). The *S* parameter (X-band) of sample was obtained by a waveguide method in a frequency range of 8.2–12.4 GHz using a vector network analyzer (VNA, Keysight N5222B, USA). The sample was pressed into a rectangle shape with a size of 22.86 mm × 10.16 mm × 2.00 mm.

Permittivity was investigated by a LCR meter (Tonghui TH2838H) equipped with a dielectric test fixture at the frequency of 20 Hz to 2 MHz at room temperature. As-received HCNFs, pure PANI, and HCNFs/PANI nanocomposites were pressed into a form of disk pellet with a diameter of 10 mm by applying a pressure of 15 MPa in a hydraulic presser, and the average thickness was about 1.00 mm. The same sample was exploited to do the electrical conductivity measurement by the four-point probe method (Keithley 2400). The temperature-dependent resistivity was studied from 70 to 300 K using a standard four-point probe technique by a 9-Tesla Physical Properties Measurement

System (PPMS, Quantum Design). The magnetoresistance was also measured on the PPMS at room temperature and the current was perpendicular to the sample.

### 3 Results and discussion

Our HCNFs/PANI nanocomposites exhibit an outstanding EMI shielding performance. The highest EMI SE values around 60–94 dB (blue circles in Fig. 1) are attained in the HCNFs/PANI nanocomposites with the HCNFs loading of 50 wt% in the X-band range at a thickness of 2.00 mm measured on the vector network analyzer. These EMI SE values are even higher than those of some metal/polymer composites in the same frequency range with the similar thickness, such as nickel/poly(vinylidene fluoride) (23 dB with a thickness of 1.95 mm) [20], nickel/cobalt/biocarbon nanofibers (made from bacterial cellulose)/paraffin wax (41.2 dB with a thickness of 2.5 mm) [21], and copper/graphite/polyvinyl chloride (70 dB with a thickness of 2.00 mm) [22]. A comparison with previously reported EMI SE values is shown in Fig. 1 and Table S1. We observe that these newly designed HCNFs/PANI nanocomposites with negative permittivity manifest a superior EMI shielding performance and could be ranked at the top of the comparison chart and table. Conversely, the PANI with a positive permittivity only possesses an EMI value of 6 dB under the same measurement condition (orange circles in Fig. 1 and Table S2).

With the purpose of understanding the high EMI shielding performance in the HCNFs/PANI nanocomposites, we first address the relationship between their microstructures and EMI SE values. In order to achieve a uniform PANI

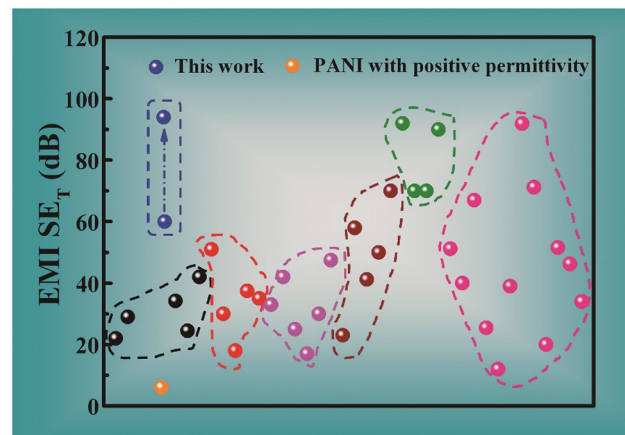


**Fig. 1** Comparison of EMI SE from literature. ● reduced graphene oxide (rGO) [45–49], ● rGO-Fe<sub>3</sub>O<sub>4</sub> [50–53], ● carbon nanotubes (CNTs) [54–59], ● metals such as nickel [21, 60], silver [61], copper [22], ● MXene [33, 62–64], ● other materials such as iron oxide [65], ferrite [66], ● PANI with positive permittivity, ● our newly designed HCNFs/PANI nanocomposites

coating outside of HCNFs, the HCNFs were firstly surface treated to form the acidic functional groups for a strong affinity with the aniline monomer [23]. Nevertheless, the commonly used chemicals for functionalizing carbon materials are concentrated on the nitric acid [24], and its strong oxidizing ability might damage the microstructures and electrical properties of carbon materials. Hence, in this work, the hexavalent chromium (Cr(VI)) aqueous solution (prepared from  $K_2Cr_2O_7$ ) was utilized to provide the carboxylic acid functional groups on the surface of HCNFs without seriously affecting their electrical properties that has already been reported in our previous work [25].

It is found that the average total EMI SE value for the as-received HCNFs is around 37 dB in the X-band range with a thickness of 2.0 mm (Fig. S1h and Table S2), whereas after Cr(VI) treatment, its average total EMI SE value becomes 35 dB without an obvious change (Fig. S1g and Table S2). This emphasizes that the Cr(VI) treatment only displays little effect on the EMI shielding performance of as-received HCNFs. Instead, the Cr(VI) treatment facilitates the polymerization of aniline monomers and uniform growth of PANI on the surface of HCNFs as indicated in SEM images (Fig. S2b–e) and TEM images (Figs. 2B and S4b–e). As a result, the HCNFs/PANI nanocomposites possess a core-sheath structure with an inner core of HCNFs and an outside sheath of PANI as expected (Figs. 2B and S4b–e), in which the internal multiple interface including the inner surface of HCNFs (Fig. 2B) and boundaries between HCNFs and PANI (marked with orange line in Fig. 2E) as well as interface between different HCNFs are created. By contrast, pure PANI exhibits a particulate-like structure (Figs. 2A, S2a and S4a), while the as-received HCNFs present a hollow fiber structure (Fig. 2C). By controlling the thickness of PANI

layers ( $175 \pm 9$ ,  $94 \pm 11$ , and  $40 \pm 5$  nm) through different HCNF loadings from 10, 20, to 40 wt%, as listed in the TEM images (Fig. S4b–d), the average total EMI SE value increases, which is approximately 35, 41, and 47 dB for the HCNFs/PANI nanocomposites at a thickness of 2.00 mm with HCNFs loading of 10, 20, and 40 wt% in the X-band range, accordingly (Fig. S1b–d and Table S2 in the supplementary material). When the loading of HCNFs is increased, the loading of PANI is decreased (for instance, the HCNF loading is 10 wt%, i.e., the PANI loading is 90 wt%), causing a declined thickness of PANI layers outside of HCNFs.

Remarkably, the HCNFs/PANI nanocomposites with 50 wt% loading of HCNFs (the thickness of PANI layer is  $25 \pm 3$  nm) reach the maximum total EMI SE value within a range of 60–94 dB in the X-band range at the same thickness. This implies that the management of microstructure and thickness of PANI layer by altering the HCNFs loadings could adjust the EMI SE values of HCNFs/PANI nanocomposites. When the HCNF loading is higher than 50 wt%, the HCNFs/PANI nanocomposites are unable to be prepared due to the high viscosity of solution. Therefore, the highest EMI SE value is achieved in the 50 wt% HCNF loading of HCNFs/PANI nanocomposites. The total EMI SE values of HCNFs/PANI nanocomposites are higher than those of pure PANI (31 dB, synthesized in the same condition with HCNFs/PANI nanocomposites) and as-received HCNFs (37 dB) under the same measurement conditions. Clearly, the core-sheath structure with internal multiple interfaces in the HCNFs/PANI nanocomposites enhances the EMI shielding performance of PANI and HCNFs. On the contrary, without Cr(VI) surface treatment, a non-uniform PANI coating with an agglomeration and entanglement is attained in the HCNFs/PANI nanocomposites, as shown in the SEM

**Fig. 2** TEM images of **A** pure PANI, **B** HCNFs/PANI nanocomposites, **C** as-received HCNFs; high-resolution TEM (HRTEM) images of **D** PANI, **E** HCNFs/PANI nanocomposites with a HCNF loading of 50 wt%, **F** HCNFs, which depicts the vivid lattice fringe of PANI, HCNFs, and HCNFs/PANI nanocomposites as well as the conspicuous interfaces between HCNFs and PANI

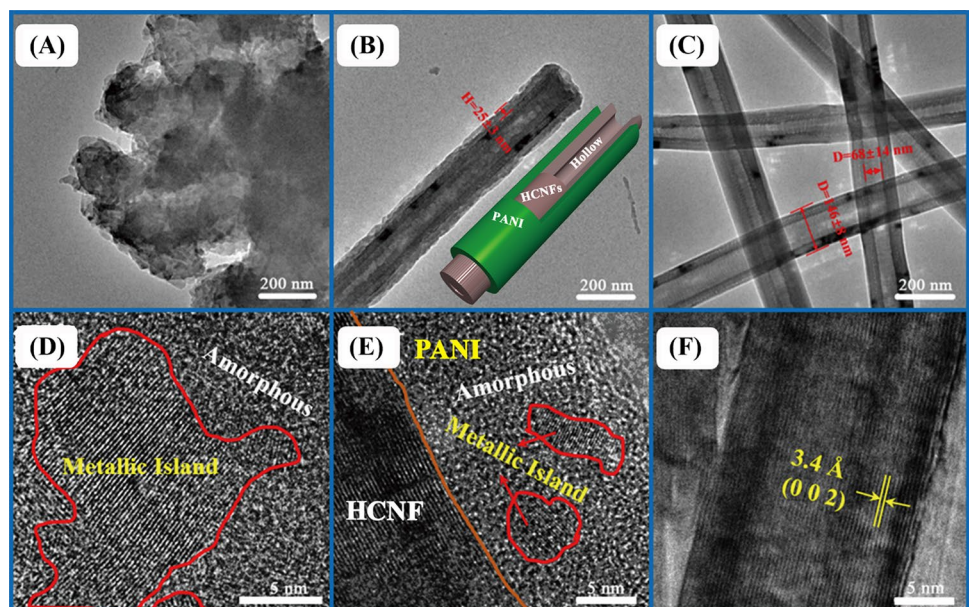


image of Fig. S3, and a relatively lower EMI SE value is observed (the average total EMI SE value for the HCNFs/PANI nanocomposites with 20 wt% loading of HCNFs with Cr(VI) treatment is 41 dB, whereas it is 36 dB for HCNFs/PANI nanocomposites without Cr(VI) treatment that is even lower than that of as-received HCNFs (37 dB). Besides, the permittivity of HCNFs/PANI nanocomposites without Cr(VI) treatment expresses a positive permittivity within the X-band range (Fig. S12f). This illustrates the importance of Cr(VI) treatment process in the manufacture of HCNFs/PANI nanocomposites.

The EMI performance is sensitive to the thickness of materials during the measurement. We have investigated this effect on the EMI SE values of HCNFs/PANI nanocomposites with 50 wt% loading of HCNFs at a thickness of 0.50, 1.00, and 2.00 mm, respectively (Fig. S16). The EMI SE values for HCNFs/PANI nanocomposites with 50 wt% loading of HCNFs at a thickness of 0.50, 1.00, and 2.00 mm are 41, 43–84, and 60–94 dB in the X-band range, respectively, Table S2. As expected, the highest EMI SE values are achieved for a 2.00-mm thickness of HCNFs/PANI nanocomposites. This is sufficient to shield almost 100% of incident EM waves since the transmittance values ( $T$ , denoting the ability of a material to shield EM waves) at 12.4 GHz is almost close to 0, Fig. S17, as predicted from the  $S$ -parameter in Eqs. (S1 and S2) [26]. In a word, the unique core-sheath microstructures and internal multiple interface scattering contribute to the high EMI SE value in the HCNFs/PANI nanocomposites.

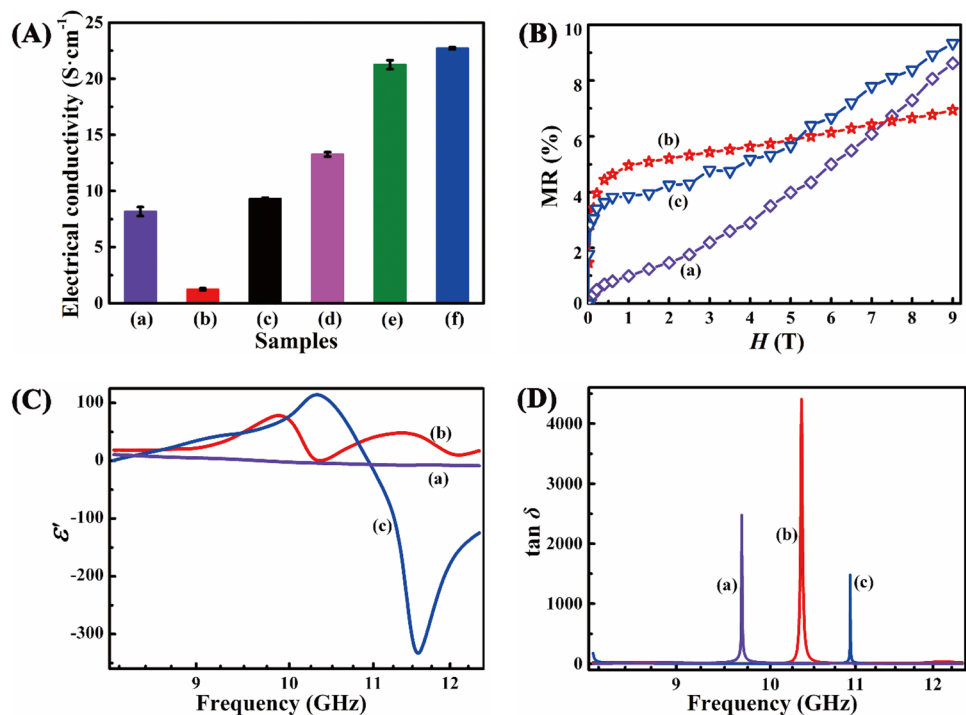
Secondly, to further analyze this superior EMI performance of HCNFs/PANI nanocomposites, the connection between their electrical conductivity and EMI SE values is explored. Principally, electrical conductivity is one of the main factors that affect the EMI shielding performance of a material. Generally, in a material with high electrical conductivity, the formed conductive network serves as a bridge to build a sufficient conducting pathway for freely transporting the mobile charge carriers that are able to reflect EM waves to achieve the EMI shielding [27]. As confirmed in the FTIR spectra (Fig. S6A), the as-fabricated PANI sheath in the HCNFs/PANI nanocomposites possesses the characteristic absorption peaks of “emeraldine” salt (ES) form, corresponding to the conductive state of PANI [28, 29]. Moreover, the clear lattice fringe in the high-resolution TEM (HRTEM) image of pure PANI and HCNFs/PANI nanocomposites (Fig. 2D, E, separately) indicates well-ordered crystalline regions (outlined in red and labeled as metallic island) in the microstructures of PANI, where the charge carriers are delocalized [30]. It is reported that the electrical conductivity of PANI is related to its degree of crystallinity [31]. The degree of crystallinity of pure PANI and PANI sheath in the HCNFs/PANI nanocomposites with a HCNF loading of 10, 20, 40, and 50 wt% evaluated from XRD patterns (Fig. S6C)

is 33.0, 41.3, 42.1, 44.6, and 46.0% based on the intensity ratio of  $I_{25.2}/I_{19.8}$  [32], respectively. The relevant electrical conductivity acquired from four-point probe method varies from  $1.23 \pm 0.10$ ,  $9.31 \pm 0.12$ ,  $13.27 \pm 0.23$ ,  $21.26 \pm 0.41$ , to  $22.71 \pm 0.10$  S  $\text{cm}^{-1}$  for the pure PANI and HCNFs/PANI nanocomposites with HCNF loading of 10, 20, 40, and 50 wt%, respectively (Table S3), which is consistent with the results from their degree of crystallinity. The tendency of electrical conductivities for these materials is consistent with the aforementioned EMI SE values obtained in Fig. S1. In other words, a higher electrical conductivity results in a larger EMI SE value [33].

The rise in electrical conductivity with increasing HCNF loadings in the HCNFs/PANI nanocomposites could also be inferred from the measurements of optical band gap ( $E_g$ ) and the density of states (DOS) at the Fermi level [ $N(E_F)$ ] (Tables S3 and S5). The  $E_g$  estimated by Eq. (S12) from the value of  $\lambda_{\text{edge}}$  (which is correlated with the  $\pi$ - $\pi^*$  interband transition in the benzoid/quinoid ring structure of PANI) [34] by ultraviolet–visible diffuse reflectance spectroscopy (UV–vis DRS), Fig. S9, is 2.31, 2.23, 2.21, 2.00, and 1.50 eV for the pure PANI and HCNFs/PANI nanocomposites with HCNF loading of 10, 20, 40, and 50 wt% (Table S3), respectively. It is concluded that a systematic decrease in the  $E_g$  with increasing HCNF loadings is observed, which is in line with the obtained degree of crystallinity and electrical conductivity. In addition, the  $N(E_F)$  of HCNFs, pure PANI, and HCNFs/PANI nanocomposites with HCNF loading of 10, 20, 40, and 50 wt% at a magnetic field of 9 T is  $4.99 \times 10^{43}$ ,  $2.12 \times 10^{40}$ ,  $2.42 \times 10^{40}$ ,  $5.71 \times 10^{40}$ ,  $2.01 \times 10^{41}$ , and  $1.39 \times 10^{41}$  ( $\text{J cm}^3$ ) $^{-1}$ , accordingly (Table S5). These values are calculated from the wave-function shrinkage model using Eqs. (S6–S10) based on the magnetoresistance (MR) that describes the resistance change of a material under an external magnetic field [35, 36]. The MR is 8.62, 6.94, and 9.33% at a magnetic field of 9 T for as-received HCNFs, pure PANI, and HCNFs/PANI nanocomposites with a HCNF loading of 50 wt%, respectively (Fig. 3B). The positive reactance of as-received HCNFs, pure PANI, and HCNFs/PANI nanocomposites in Fig. S10 suggests an inductance characteristic in these materials, implying the formation of conductive networks [37] in accordance with their high electrical conductivity.

Furthermore, the dielectric property of HCNFs, pure PANI, and HCNFs/PANI nanocomposites is studied to explore the relationship between permittivity, electrical conductivity, and EMI shielding performance. The permittivity details the nature of electrostatic energy savings and losses under the action of an electric field [38]. In this work, we have studied the permittivity of as-received HCNFs, pure PANI, and HCNFs/PANI nanocomposites in both the X-band range (calculated based on the Nicholson-Ross-Weir method) and the low frequency range (20 Hz–2 MHz),

**Fig. 3** **A** Electrical conductivity of the HCNFs/PANI nanocomposites with HCNF loading of (a) 10, (b) 20, (c) 40, (d) 50%, and (e) pure PANI; **B** room temperature magnetoresistance; **C** frequency dependent  $\epsilon'$ ; **D** frequency dependent  $\tan \delta$  of (a) as-received HCNFs, (b) pure PANI, and (c) HCNFs/PANI nanocomposites with a HCNFs loading of 50 wt%



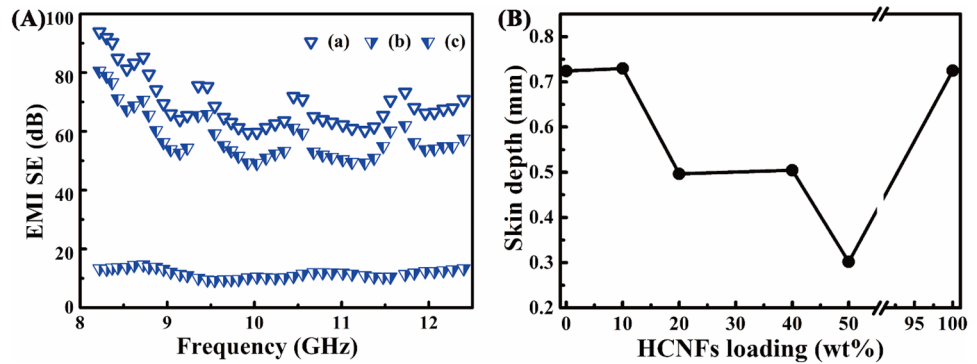
separately. It is observed that in the low frequency range, both HCNFs and HCNFs/PANI nanocomposites exhibit the negative real permittivity ( $\epsilon'$ , Fig. S11A), whereas the real permittivity of PANI could be either negative or positive by controlling the concentrations of doped acid PTSA during the fabrication (Fig. S13). It is found that the PANI doped with 3.75 mmol of PTSA possesses a positive real permittivity (Fig. S13A) and an electrical conductivity of  $5.2 \times 10^{-4} \pm 1 \times 10^{-6} \text{ S cm}^{-1}$ , while PANI doped with 15 mmol of PTSA displays a negative real permittivity (Fig. S11A) and an electrical conductivity of  $1.23 \pm 0.11 \text{ S cm}^{-1}$ . In theory, the low-frequency negative permittivity is often explained by the creation of continuous conductive pathways in a material that originates from the plasma oscillations of delocalized charge carriers on the basis of Drude model, i.e., it is associated with the electrical conductivity of material [15]. Our results verify the relationship between negative permittivity and electrical conductivity. According to the Drude model, the plasma frequency ( $\omega_p$ ) is given by  $\omega_p = \sqrt{n_{\text{eff}}e^2/m_{\text{eff}}\epsilon_0}$ , where  $\epsilon_0$  is the permittivity of vacuum ( $8.85 \times 10^{-12} \text{ F m}^{-1}$ ),  $n_{\text{eff}}$  is the effective concentration of delocalized electrons,  $m_{\text{eff}}$  is the effective weight of electron, and  $e$  is the electron charge ( $1.6 \times 10^{-19} \text{ C}$ ). In a metal, the  $\omega_p$  corresponds to the switching frequency where the permittivity changes from negative to positive, which depends on the  $n_{\text{eff}}$ , that is, the electrical conductivity of material. On the contrary, in the X-band range, the PANI doped with 15 mmol of PTSA depicts a positive permittivity (Fig. 3C-b), and the permittivity for as-received HCNFs (Fig. 3C-a)

and HCNFs/PANI nanocomposites is changed from positive to negative (Figs. 3C and S12). Most notably, the HCNFs/PANI nanocomposites with 50 wt% loading of HCNFs show a maximum negative permittivity up to  $-332.8$  (Fig. 3C-c).

The relationship between permittivity vs. frequency in the X-band range could also be further clarified by analyzing an interband transition using the Lorentz effect or Lorentz model, Eq. (S15) [39], which describes the dielectric dispersion resulting from the dielectric resonance polarization [40]. In this situation, the Drude model could not explain the phenomenon since the Lorentz oscillators are responsible for this effect. Owing to the Lorentz effect, the real permittivity of all the HCNFs/PANI nanocomposites is altered from positive to negative in the X-band range. Collectively, based on the aforementioned relationship between electrical conductivity and permittivity, the highest EMI SE values of 60–94 dB in the 50 wt% HCNF loading of HCNFs/PANI nanocomposites (Fig. S1c) are linked to their unique dielectric properties, electrical conductivity, and microstructures.

The EMI shielding mechanism from reflection ( $SE_R$ ) and absorption ( $SE_A$ ) for as-received HCNFs, pure PANI, and HCNFs/PANI nanocomposites is estimated from Eq. (S5) and laid out in Figs. 4A, S15B, C, and Table S2. The existence of interfaces between PANI and HCNFs as well as crystalline ranges in the PANI microstructures (Fig. 2E) causes multiple scattering inside of HCNFs/PANI nanocomposites, further fading EM waves [41]. Figure 4B shows the skin depth (which is the depth that the EM waves

**Fig. 4** **A** EMI  $SE_T$  (a) and corresponding reflection ( $SE_R$ , b) and absorption ( $SE_A$ , c) for HCNFs/PANI nanocomposites with 50 wt% loading of HCNFs; **B** skin depth at 12.4 GHz for pure PANI, HCNFs/PANI nanocomposites, and as-received HCNFs



can penetrate in and is an important parameter to assess the EMI shielding performance of a material [42–44]) at 12.4 GHz of the HCNFs/PANI nanocomposites with variable loadings of HCNFs. It is noticed that the skin depth for HCNFs/PANI nanocomposites is reduced from 0.72 to 0.30 mm with increasing HCNF loading from 0 (i.e., pure PANI) to 50 wt%, expressing the same trend as the variation of electrical conductivity for the HCNFs/PANI nanocomposites (Table S3). The skin depth for all the products is smaller than their thickness (2.00 mm), which is good for attaining relatively higher EMI SE values in HCNFs/PANI nanocomposites.

Overall, this superior EMI shielding phenomenon in the HCNFs/PANI nanocomposites is possibly attributed to the proposed mechanism as drawn in Fig. 5. The EMI shielding performance originates from their outstanding core-sheath architecture, high electrical conductivity, and unique negative permittivity. The negative permittivity could provide these nanocomposites with an excellent conductive pathway. As the incident EM waves strike their surface, some of waves are reflected as a result of high electrical conductivity. The rest penetrates inside the core-sheath microstructures, where the internal interfaces serve as scattering centers and enable multiple scattering of EM waves, inducing the attenuation of EM waves until they are totally absorbed in the microstructures.

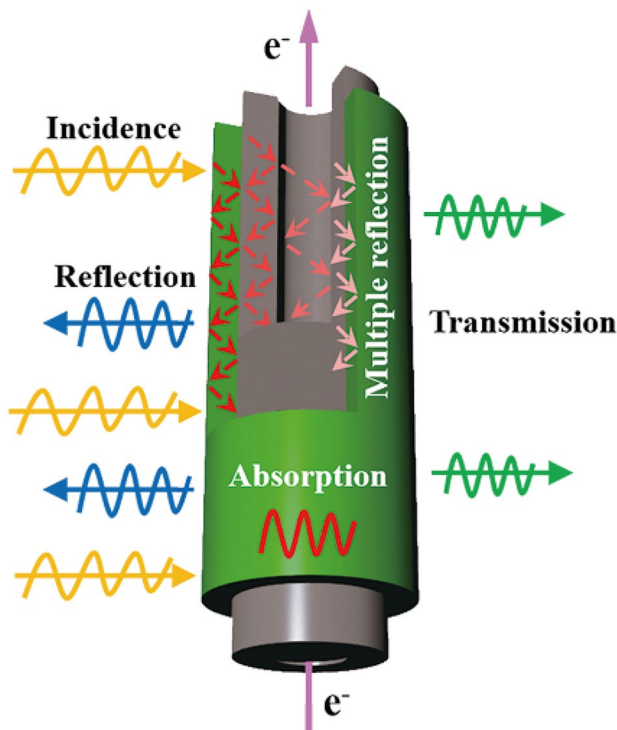


**Fig. 5** Proposed EMI shielding mechanism in HCNFs/PANI nanocomposites

## 4 Conclusion

In summary, an exceptional adjustable core-sheath HCNFs/PANI nanocomposite with negative permittivity has been demonstrated for EMI shielding. Although their electrical conductivity ( $21.26 \pm 0.41 \text{ S cm}^{-1}$  for HCNFs/PANI nanocomposites with 50 wt% loading) is lower than that of common metals ( $10^4$ – $10^5 \text{ S cm}^{-1}$ ), they manifest a comparable EMI shielding performance to metals (EMI SE value of 60–94 dB in the X-band range) arising from their core-sheath microstructures (internal multiple scattering) and negative permittivity (up to  $-332.8$ ) in the X-band range. This study opens a new avenue to connect the EMI shielding performance with the microstructure construction of polymer nanocomposites and negative permittivity, which offer many advantages over normal metals. This work may provide a new insight for designing the polymer nanocomposites with negative permittivity for reaching the extraordinary EMI shielding.

**Supplementary Information** The online version contains supplementary material available at <https://doi.org/10.1007/s42114-022-00538-8>.

**Funding** The authors are grateful for the support and funding from Shanghai Rising-Star Program (19QA1409400). This work is supported by Shanghai Science and Technology Commission (19DZ2271500). The authors also acknowledged the financial support of Taif University

Researchers Supporting Project number (TURSP-2020/220). The authors thank Mr. Bo Xiao from Beijing Huace Testing Instrument Co., Ltd. (Beijing) for the electrical conductivity measurements. The authors also thank Beijing Zhongkebaice Technology Service Co., Ltd. for TEM measurements.

## Declarations

**Conflict of interest** The authors declare no competing interests.

## References

1. Yan DX, Pang H, Li B, Vajtai R, Xu L, Ren PG, Wang JH, Li ZM (2015) Structured reduced graphene oxide/polymer composites for ultra-efficient electromagnetic interference shielding. *Adv Funct Mater* 25:559–566
2. Hao S, Shen Y, Wu H, Meng J, Xie L, Wen T, Ning G, Liu J, Zhang Y, Xu H (2018) Modulatory effects of the composition and structure on the osteogenic enhancement for superparamagnetic scaffolds. *Eng Sci* 4:100–110
3. Han MK, Yin XW, Hantanasirisakul K, Li XL, Iqbal A, Hatter CB, Anasori B, Koo CM, Torita T, Soda Y, Zhang LT, Cheng LF, Gogotsi Y (2019) Anisotropic MXene aerogels with a mechanically tunable ratio of electromagnetic wave reflection to absorption. *Adv Opt Mater* 7:1900267
4. Kulkarni G, Kandesar P, Velhal N, Phadtare V, Jatrakr A, Shinde SK, Kim DY, Puri V (2019) Exceptional electromagnetic interference shielding and microwave absorption properties of room temperature synthesized polythiophene thin films with double negative characteristics (DNG) in the Ku-band region. *Chem Eng J* 355:196–207
5. Zhu J, Wei S, Zhang L, Mao Y, Ryu J, Haldolaarachchige N, Young DP, Guo Z (2011) Electrical and dielectric properties of polyaniline- $\text{Al}_2\text{O}_3$  nanocomposites derived from various  $\text{Al}_2\text{O}_3$  nanostructures. *J Mater Chem* 21:3952–3959
6. Xiao Y, He Y, Wang R, Lei Y, Yang J, Qi X, Wang Y (2022) Mussel-inspired strategy to construct 3D silver nanoparticle network in flexible phase change composites with excellent thermal energy management and electromagnetic interference shielding capabilities. *Compos Part B Eng* 239:109962
7. Liang C, Qiu H, Han Y, Gu H, Song P, Wang L, Kong J, Cao D, Gu J (2019) Superior electromagnetic interference shielding 3D graphene nanoplatelets/reduced graphene oxide foam/epoxy nanocomposites with high thermal conductivity. *J Mater Chem C* 7:2725–2733
8. Xie P, Zhang Z, Liu K, Qian L, Dang F, Liu Y, Fan R, Wang X, Dou S (2017) C/SiO<sub>2</sub> meta-composite: overcoming the  $l/a$  relationship limitation in metamaterials. *Carbon* 125:1–8
9. Cheng CB, Jiang YL, Sun X, Shen JX, Wang TL, Fan GH, Fan RH (2020) Tunable negative permittivity behavior and electromagnetic shielding performance of silver/silicon nitride metamaterials. *Compos Part A Appl Sci Manuf* 130:105753
10. Gu H, Xu X, Dong M, Xie P, Shao Q, Fan R, Liu C, Wu S, Wei R, Guo Z (2019) Carbon nanospheres induced high negative permittivity in nanosilver-polydopamine metamaterials. *Carbon* 147:550–558
11. Zhu J, Wei S, Zhang L, Mao Y, Ryu J, Mavinakuli P, Karki AB, Young DP, Guo Z (2010) Conductive polypyrrole/tungsten oxide metamaterials with negative permittivity. *J Phys Chem C* 114:16335–16342
12. Sun K, Xie P, Wang Z, Su T, Shao Q, Ryu J, Zhang X, Guo J, Shankar A, Li J, Fan R, Cao D, Guo Z (2017) Flexible polydimethylsiloxane/multi-walled carbon nanotubes membranous metamaterials with negative permittivity. *Polymer* 125:50–57
13. Zhu J, Wei S, Ryu J, Guo Z (2011) Strain-sensing elastomer/carbon nanofiber “metacomposites.” *J Phys Chem C* 115:13215–13222
14. Gu H, Zhang H, Ma C, Lyu S, Yao F, Liang C, Yang X, Guo J, Guo Z, Gu J (2017) Polyaniline assisted uniform dispersion for magnetic ultrafine barium ferrite nanorods reinforced epoxy metamaterials with tailorable negative permittivity. *J Phys Chem C* 121:13265–13273
15. Zhang C, Shi Z, Mao F, Yang C, Zhu X, Yang J, Zuo H, Fan R (2018) Flexible Polyimide nanocomposites with dc bias induced excellent dielectric tunability and unique nonpercolative negative- $k$  toward intrinsic metamaterials. *ACS Appl Mater Interfaces* 10:26713–26722
16. Yao X, Kou X, Qiu J (2016) Multi-walled carbon nanotubes/polyaniline composites with negative permittivity and negative permeability. *Carbon* 107:261–267
17. Cai J, Wang W, Pan D, Young DP, Gu H, Guo Z (2020) Electrical transport in polyaniline–barium ferrite nanocomposites with negative giant magnetoresistance. *J Phys Chem C* 124:22646–22655
18. Yao F, Xie W, Yang M, Zhang H, Gu H, Du A, Naik N, Young DP, Lin J, Guo Z (2021) Interfacial polymerized copolymers of aniline and phenylenediamine with tunable magnetoresistance and negative permittivity. *Mater Today Phys* 21:100502
19. Lu Z, Ma L, Tan J, Wang H, Ding X (2016) Transparent multilayer graphene/polyethylene terephthalate structures with excellent microwave absorption and electromagnetic interference shielding performance. *Nanoscale* 8:16684–16693
20. Gargama H, Thakur AK, Chaturvedi SK (2015) Polyvinylidene fluoride/nickel composite materials for charge storing, electromagnetic interference absorption, and shielding applications. *J Appl Phys* 117:224903
21. Huang X, Dai B, Ren Y, Xu J, Zhu P (2015) Preparation and study of electromagnetic interference shielding materials comprised of Ni-Co coated on web-like biocarbon nanofibers via electroless deposition. *J Nanomater* 2015:320306
22. Al-Ghamdi AA, El-Tantawy F (2010) New electromagnetic wave shielding effectiveness at microwave frequency of polyvinyl chloride reinforced graphite/copper nanoparticles. *Compos Part A Appl Sci Manuf* 41:1693–1701
23. Gu H, Zhang H, Gao C, Liang C, Gu J, Guo Z (2018) New functions of polyaniline. *ES Mater Manuf* 1:3–12
24. Worsley KA, Kalinina I, Bekyarova E, Haddon RC (2009) Functionalization and dissolution of nitric acid treated single-walled carbon nanotubes. *J Am Chem Soc* 131:18153–18158
25. Gu H, Rapole SB, Huang Y, Cao D, Luo Z, Wei S, Guo Z (2013) Synergistic interactions between multi-walled carbon nanotubes and toxic hexavalent chromium. *J Mater Chem A* 1:2011–2021
26. Verma M, Chauhan SS, Dhawan SK, Choudhary V (2017) Graphene nanoplatelets/carbon nanotubes/polyurethane composites as efficient shield against electromagnetic polluting radiations. *Compos B* 120:118–127
27. Jia Y, Li K, Xue L, Ren J, Zhang S, Li H (2017) Mechanical and electromagnetic shielding performance of carbon fiber reinforced multilayered (PyC-SiC)<sub>n</sub> matrix composites. *Carbon* 111:299–308
28. Gu H, Zhang H, Lin J, Shao Q, Young DP, Sun L, Shen TD, Guo Z (2018) Large negative giant magnetoresistance at room temperature and electrical transport in cobalt ferrite-polyaniline nanocomposites. *Polymer* 143:324–330
29. Ingle R, Shaikh S, Bhujbal P, Pathan H, Tabhane V (2020) Polyaniline doped with protonic acids: optical and morphological studies. *ES Mater Manuf* 8:54–59
30. Guo J, Chen Z, Abdul W, Kong J, Khan MA, Young DP, Zhu J, Guo Z (2021) Tunable positive magnetoresistance of magnetic polyaniline nanocomposites. *Adv Compos Hybrid Mater* 4:534–542
31. Sezen-Edmonds M, Khlyabich PP, Loo Y-L (2017) Tuning the magnitude and the polarity of the piezoresistive response of



- polyaniline through structural control. *ACS Appl Mater Interfaces* 9:12766–12772
32. Xu X, Fu Q, Gu H, Guo Y, Zhou H, Zhang J, Pan D, Wu S, Dong M, Guo Z (2020) Polyaniline crystalline nanostructures dependent negative permittivity metamaterials. *Polymer* 188:122129
  33. Shahzad F, Alhabeab M, Hatter CB, Anasori B, Man Hong S, Koo CM, Gogotsi Y (2016) Electromagnetic interference shielding with 2D transition metal carbides (MXenes). *Science* 353:1137–1140
  34. Xie W, Yao F, Gu H, Du A, Lei Q, Naik N, Guo Z (2022) Magneto-resistive and piezoresistive polyaniline nanoarrays in-situ polymerized surrounding magnetic graphene aerogel. *Adv Compos Hybrid Mater*. <https://doi.org/10.1007/s42114-42021-00413-y>
  35. Gu H, Guo J, Wei H, Guo S, Liu J, Huang Y, Mojammel AK, Wang X, David PY, Wei S, Guo Z (2015) Strengthened magneto-resistive epoxy nanocomposite papers derived from synergistic nanomagnetite-carbon nanofiber nanohybrids. *Adv Mater* 27:6277–6282
  36. Gao C, Yang M, Xie W, Zhang H, Gu H, Du A, Shi Z, Guo Y, Zhou H, Guo Z (2021) Adjustable magnetoresistance in semi-conducting carbonized phthalonitrile resin. *Chem Commun* 57:9894–9897
  37. Xie P, Wang Z, Sun K, Cheng C, Liu Y, Fan R (2017) Regulation mechanism of negative permittivity in percolating composites via building blocks. *Appl Phys Lett* 111:112903
  38. Zhou Y, Wang P, Ruan G, Xu P, Ding Y (2021) Synergistic effect of p[MPEGMA-IL] modified graphene on morphology and dielectric properties of PLA/PCL blends. *ES Mater Manuf* 11:20–29
  39. Wang Z, Sun K, Xie P, Liu Y, Fan R (2017) Generation mechanism of negative permittivity and Kramers-Kronig relations in BaTiO<sub>3</sub>/Y<sub>3</sub>Fe<sub>5</sub>O<sub>12</sub> multiferroic composites. *J Phys Condens Matter* 29:365703
  40. Oughstun KE, Cartwright NA (2003) On the Lorentz-Lorenz formula and the Lorentz model of dielectric dispersion. *Opt Express* 11:1541–1546
  41. Zhao B, Park CB (2017) Tunable electromagnetic shielding properties of conductive poly(vinylidene fluoride)/Ni chain composite films with negative permittivity. *J Mater Chem C* 5:6954–6961
  42. Wang Y, Gu F, Ni L, Liang K, Marcus K, Liu S, Yang F, Chen J, Feng Z (2017) Easily fabricated and lightweight PPy/PDA/AgNW composites for excellent electromagnetic interference shielding. *Nanoscale* 9:18318–18325
  43. Cheng H, Pan Y, Wang X, Liu C, Shen C, Schubert DW, Guo Z, Liu X (2022) Ni flower/MXene-melamine foam derived 3D magnetic/conductive networks for ultra-efficient microwave absorption and infrared stealth. *Nano-Micro Lett* 14:63
  44. Sotiropoulos A, Koulouridis S, Masouras A, Kostopoulos V, Anastassiou HT (2021) Carbon nanotubes films in glass fiber polymer matrix forming structures with high absorption and shielding performance in X-Band. *Compos Part B Eng* 217:108896
  45. Ling J, Zhai W, Feng W, Shen B, Zhang J, Zheng W (2013) Facile preparation of lightweight microcellular polyetherimide/graphene composite foams for electromagnetic interference shielding. *ACS Appl Mater Interfaces* 5:2677–2684
  46. Wen B, Wang XX, Cao WQ, Shi HL, Lu MM, Wang G, Jin HB, Wang WZ, Yuan J, Cao MS (2014) Reduced graphene oxides: the thinnest and most lightweight materials with highly efficient microwave attenuation performances of the carbon world. *Nanoscale* 6:5754–5761
  47. Yuan B, Yu L, Sheng L, An K, Zhao X (2012) Comparison of electromagnetic interference shielding properties between single-wall carbon nanotube and graphene sheet/polyaniline composites. *J Phys D Appl Phys* 45:235108
  48. Shahzad SYu, Kumar P, Lee J, Kim Y, Hong SM, Koo CM (2015) Sulfur doped graphene/polystyrene nanocomposites for electromagnetic interference shielding. *Compos Struct* 133:1267–1275
  49. Umrao S, Gupta TK, Kumar S, Singh VK, Sultania MK, Jung JH, Oh IK, Srivastava A (2015) Microwave-assisted synthesis of boron and nitrogen Co-doped reduced graphene oxide for the protection of electromagnetic radiation in Ku-band. *ACS Appl Mater Interfaces* 7:19831–19842
  50. Singh AP, Mishra M, Sambyal P, Gupta BK, Singh BP, Chandra A, Dhawan SK (2014) Encapsulation of g-Fe<sub>2</sub>O<sub>3</sub> decorated reduced graphene oxide in polyaniline core-shell tubes as an exceptional tracker for electromagnetic environmental pollution. *J Mater Chem A* 2:3581–3593
  51. Singh K, Ohlan A, Pham VH, Balasubramanian R, Varshney S, Jang J, Hur SH, Choi WM, Kumar M, Dhawan SK, Kong BS, Chung JS (2013) Nanostructured graphene/Fe<sub>3</sub>O<sub>4</sub> incorporated polyaniline as a high performance shield against electromagnetic pollution. *Nanoscale* 5:2411–2420
  52. Shen B, Zhai W, Tao M, Ling J, Zheng W (2013) Lightweight, multifunctional polyetherimide/graphene@Fe<sub>3</sub>O<sub>4</sub> composite foams for shielding of electromagnetic pollution. *ACS Appl Mater Interfaces* 5:11383–11391
  53. Singh AP, Mishra M, Hashim DP, Narayanan TN, Hahm MG, Kumar P, Dwivedi J, Kedawat G, Gupta A, Singh BP, Chandra A, Vajtai R, Dhawan SK, Ajayan PM, Gupta BK (2015) Probing the engineered sandwich network of vertically aligned carbon nanotube-reduced graphene oxide composites for high performance electromagnetic interference shielding applications. *Carbon* 85:79–88
  54. Chen Y, Zhang HB, Yang Y, Wang M, Cao A, Yu ZZ (2016) High-performance epoxy nanocomposites reinforced with three-dimensional carbon nanotube sponge for electromagnetic interference shielding. *Adv Funct Mater* 26:447–455
  55. Gupta A, Choudhary V (2011) Electromagnetic interference shielding behavior of poly(trimethylene terephthalate)/multi-walled carbon nanotube composites. *Compos Sci Technol* 71:1563–1568
  56. Huang Y, Li N, Ma Y, Du F, Li F, He X, Lin X, Gao H, Chen Y (2007) The influence of single-walled carbon nanotube structure on the electromagnetic interference shielding efficiency of its epoxy composites. *Carbon* 45:1614–1621
  57. Liu Z, Bai G, Huang Y, Ma Y, Du F, Li F, Guo T, Chen Y (2007) Reflection and absorption contributions to the electromagnetic interference shielding of single-walled carbon nanotube/polyurethane composites. *Carbon* 45:821–827
  58. Song Q, Ye F, Yin X, Li W, Li H, Liu Y, Li K, Xie K, Li X, Fu Q, Cheng L, Zhang L, Wei B (2017) Carbon nanotube-multilayered graphene edge plane core-shell hybrid foams for ultrahigh-performance electromagnetic-interference shielding. *Adv Mater* 29:1701583
  59. Zhang K, Li GH, Feng LM, Wang N, Guo J, Sun K, Yu KX, Zeng JB, Li T, Guo MW (2017) Ultralow percolation threshold and enhanced electromagnetic interference shielding in poly(l-lactide)/multi-walled carbon nanotube nanocomposites with electrically conductive segregated networks. *J Mater Chem C* 5:9359–9369
  60. Luo J, Wang L, Huang X, Li B, Guo Z, Song X, Lin L, Tang LC, Xue H, Gao J (2019) Mechanically durable, highly conductive, and anticorrosive composite fabrics with excellent self-cleaning performance for high-efficiency electromagnetic interference shielding. *ACS Appl Mater Interfaces* 11:10883–10894
  61. Fang F, Li YQ, Xiao HM, Hu N, Fu SY (2016) Layer-structured silver nanowire/polyaniline composite film as a high performance X-band EMI shielding material. *J Mater Chem C* 4:4193–4203
  62. Wang QW, Zhang HB, Liu J, Zhao S, Xie X, Liu L, Yang R, Koratkar N, Yu ZZ (2019) Multifunctional and water-resistant mxene-decorated polyester textiles with outstanding electromagnetic interference shielding and joule heating performances. *Adv Funct Mater* 29:1806819
  63. Li X, Yin X, Liang S, Li M, Cheng L, Zhang L (2019) 2D carbide MXene Ti<sub>2</sub>CTX as a novel high-performance electromagnetic interference shielding material. *Carbon* 146:210–217

64. Liu J, Zhang HB, Sun R, Liu Y, Liu Z, Zhou A, Yu ZZ (2017) Hydrophobic, flexible, and lightweight mxene foams for high-performance electromagnetic-interference shielding. *Adv Mater* 29:1702367
65. Varshney S, Ohlan A, Jain VK, Dutta VP, Dhawan SK (2014) In situ synthesis of polypyrrole- $\gamma$ - $\text{Fe}_2\text{O}_3$ -fly ash nanocomposites for protection against EMI pollution. *Ind Eng Chem Res* 53:14282–14290
66. Xu P, Han X, Wang C, Zhao H, Wang J, Wang X, Zhang B (2008) Synthesis of electromagnetic functionalized barium ferrite nanoparticles embedded in polypyrrole. *J Phys Chem B* 112:2775–2781

**Publisher's Note** Springer Nature remains neutral with regard to jurisdictional claims in published maps and institutional affiliations.

Springer Nature or its licensor holds exclusive rights to this article under a publishing agreement with the author(s) or other rightsholder(s); author self-archiving of the accepted manuscript version of this article is solely governed by the terms of such publishing agreement and applicable law.